This article is published on :

Geophys. J. Int., 145, 336-348, 2001.

Analyses of the stress field in southeastern France from earthquake focal mechanisms.

Emmanuel BAROUX[1,3], Nicole BÉTHOUX[2] and Olivier BELLIER[1,4]

1: UMR ORSAYTERRE (UMR CNRS 8616), Bat 509, Centre d'Orsay, 91405 Orsay cedex, France.

2: UMR GEOSCIENCES-AZUR (UMR CNRS 6526), Rue A. Einstein, Sophia-Antipolis, 06560 Valbonne, France.

3: now at ING - Via di Vigna Murata, 605 - 00143 Roma - Italy

4: now at CEREGE - BP 80, Europole Méditerranéen de l'Arbois - 13545 Aix en Provence Cedex 4 - France

Short Title: *SE France stress field from focal mechanisms.*

Summary

Due to the apparent deformation field heterogeneity, the stress regimes around the Provence block, from the fronts of the Massif Central and Alpine range up to the Ligurian Sea, were not well defined. To improve the understanding of the SE France stress field, we determine new earthquake focal mechanisms and we compute the present-day stress states by inversion of the 89 available focal mechanisms around the Provence domain, including the 17 new ones calculated in the current study. This study provides evidence of 6 different deformation domains around the Provence block with different tectonic regimes. On a regional scale, we identify three zones characterised by significantly different stress regimes: a western one affected by an extensional stress (normal faulting) regime, a southeastern one characterised by a compressional stress (reverse to strike-slip faulting) regime with NNW- to WNW-trending σ_1 and a northeastern one, i.e., the Digne nappe front, marked by an NE-trending compression. Note that the Digne nappe back domain is controlled by an extensional regime that is deforming the western alpine core. This extensional regime could be a response to buoyancy forces related to the Alpine high topography. The stress regimes in the southeast of the Argentera Massif and around the Durance fault are consistent with a coherent NNW-trending σ_1 that implies a left-lateral component of the active reverse oblique-slip of the Moyenne Durance Fault. In the Rhone Valley, an E-trending extension characterises the tectonic regime that implies a normal component of the present-day Nîmes fault displacement.

This study provides evidence for short-scale variation of the stress states that reflect abrupt change in the boundary force influences on upper crustal fragments (blocks). These spatial stress changes around the Provence block result from the coeval influence of forces applied at both its extremities, i.e., in the north-east, the Alpine front push and in the southeast, the northward African plate drift. Besides these boundary forces, the influence of the mantle plume under the Massif Central can be superimposed along the western block boundary.

Key Words: Southeastern France, focal mechanisms, seismotectonics, stress field.

I - Introduction

In the Southeastern France domain, geomorphic and tectonic analyses provide evidence for localised deformation along individual fault zones like the Nîmes and Moyenne Durance faults, and the Digne and Castellane nappes (e.g., Combes 1984; Ritz 1991) (Fig. 1). The Nîmes and Moyenne Durance faults are seismically active on three time scales: by paleoseismicity, historical seismicity and instrumental seismicity. The Moyenne Durance Fault is probably the most active fault in the studied zone. It is characterised by four historical earthquakes (MSK Intensity > VII) since 1509 (Levret *et al.* 1994) and by a paleoseismic event which produced more than 1 m reverse faulting displacement, between 27.000 BP and 9.000 BP (Sébrier *et al.* 1997). Paradoxically, the regional instrumental seismicity is low while geodetic results imply that the present-day total left-lateral strike-slip rates on both the Moyenne Durance and Nîmes faults is unlikely to exceed 2 mm/yr (Ferhat *et al.* 1998). In addition, a previous analysis of focal mechanisms for France (Nicolas *et al.* 1990) provided evidence for heterogeneous deformations in SE France. In this region the computed focal mechanisms were sparse and poorly defined due to the low-density of seismic stations. Through inversion of focal mechanisms, Delouis *et al.* (1993) determined the stress field in different French domains. For the southwestern Alps and Provence, the stress state has not been computed due to both, the lack of seismic events, and the heterogeneous deformation related to the rapid spatial variation of the stress field. However, thanks to the increasing development of seismic networks in France, the seismicity imaging of SE France can now be improved. The aim of this paper is to analyse the SE France stress field, i.e., mainly around the Provence domain, from the fronts of the Massif Central and Alpine range up to the Ligurian Sea. For this objective, we have determined new earthquake focal mechanisms and we have computed the present-day stress states by inversion of the 89 available focal mechanisms around this Provence domain.

II - The seismological data

A- The seismological network

Nowadays, dense networks distributed throughout France monitor the seismicity of southeastern France. Fig. 2 displays the location of the stations used for this study. They have come into operation progressively over time. Most of the LDG[*] stations were installed nearly forty years ago, and the ReNaSS[*] network of Nice and Provence in 1983, whereas the stations of the Massif Central and Pyrenees mountain ranges were installed between 1983 and 1998. The Durance valley network, installed by the IPSN[*] with 13 stations, has been progressively operated since 1993. We also benefit from all the data available from the IGG[*] network and some data recorded by the SISMALP[*] network for events between 1993 and 1998.

Consequently, the focal solution is best defined for the more recent events, because the solution accuracy is directly linked to the number of data available, the network geometry and the source-stations distance. Nevertheless we could compute focal mechanisms for events which occurred since 1980. For the oldest events, the available data allowed the determination of the mechanism types (normal, thrusting or strike-slip faulting) and the approximate trend for the P and T axes. The lack of seismicity recorded in the last few years led us to take into account also poorly defined solutions, which will be considered to be less confident than the others.

[*] LDG: Laboratoire de Détection et Géophysique, Bryères-le-Chatel, France - ReNaSS: Réseau National de Surveillance Sismique, Strasbourg, France - IPSN : Institut de Protection et de Sureté Nucléaire, Fontenay-aux-Roses, France. IGG: Istituto Geofisico e Geodetico, presently Istittuto di Scienze della Terra, Genova, Italy - SISMALP : Réseau de Surveillance de la Sismicité Alpine, Grenoble, France.

B - Location procedure and computation of the take-off angles.

All the earthquakes of southeastern France, which occurred between 1962 and 1992, were located and studied using a code written to take into account secondary arrivals and different crustal models according to the area of the epicentre (see details in Nicolas *et al.* 1998). In order to obtain a file with the take-off angles, we re-located these events using Hypo 71 software (Lee & Lahr 1975), with the same crustal model and event depths as in the previous study, using secondary arrivals. For the most recent events, the availability of nearby stations permitted a reliable hypocentral location. Moreover, some earthquakes with epicentral distance less than twice the focal depth warrant this location quality. For the others, the location accuracy was evaluated using the location of rock bursts of a coal mine located just in the south of the Durance valley (Gardanne mine, Fig. 2). Nicolas *et al.* (1998) estimated the accuracy of about +/- 1 km for the epicentral parameters and 5 km for the depth, for events after 1983, when there was an increase of the seismic network density. The magnitude range of the 54 compiled events is 2.9 to 4.7 (Ml magnitude computed by the LDG network), but the average magnitude is around 3.0. In this paper, we examine only the 17 events with the most stable focal mechanisms. Their magnitudes range from 3.0 to 4.7. The location of these events, with focal mechanisms, is reported in Table 1 and displayed on Fig. 1.

C - New Earthquake fault-plane solutions

Reliable focal mechanisms have been computed in two steps. First, the nodal planes were graphically determined by displaying the seismic rays with the corresponding polarity on a stereogram, using a code added to Hypo71 software. Second, the focal mechanisms were computed by means of the FPFIT code (Reasenberg & Oppenheimer 1985) which systematically searches the solution space for the double couple fault plane solutions that best fit, in a least-squares sense, a given set of observed first motion polarities. This method may determine several solutions with related uncertainties for both nodal planes. The final step of this methodology is to verify that the previously graphically-determined solution is close to one of the solutions provided by the FPFIT code. Generally, the automatic FPFIT research includes the graphically-determined solution among the multiple solutions and for the best-constrained mechanisms only one solution is obtained by both methods. Nevertheless, in two cases, we chose the graphical solution (Fig. 3). For the event n5 (880805) our graphical solution is very close to one of the multiple solution computed by FPFIT code. However, we select the graphical solution because it is in better agreement with the local geology. The second case corresponds to the magnitude 3.6 event n15 (971106). This earthquake and the magnitude 4.7 event n14 (971031) are located around the town of Allos, in the northeastern part of the studied region . These earthquakes were analysed by Sue *et al. (*1999) in parallel with our study. These authors computed the focal solution with only the SISMALP network, with stations very close to the epicentres; we studied the same events with the other networks. For our own set of data, FPFIT provided only one solution that corresponds to a pure inverse mechanism, whereas our graphical solution was a transpressional mechanism (see Fig. 3). This solution is very close to the solution recently published by Sue *et al. (*1999) that has been obtained with a dense local network. Conversely, for the n14 event, we kept the FPFIT solution because it provides a similar tectonic result than the solution of Sue *et al. (*1999), i.e., same fault kinematics, and it is in good agreement with our n15 solution (see Fig. 1).

Consequently, both methods (graphical method and FPFIT code) are complementary and help in the selection of a reliable focal mechanism in case of multiple focal solutions.

In the current study we have determined 17 new earthquake focal mechanisms of which we report the selected solutions in Table 1 and on Fig. 1. The detailed solutions are reported in Fig. 4.

D - The bibliographic focal mechanisms.

Focal mechanisms from other events which occurred in the studied region have already been determined by different authors (Bossolasco *et al.* 1972; Fréchet & Pavoni 1979; Béthoux *et al.* 1988; Nicolas *et al.* 1990; Deverchère *et al.* 1991; Béthoux *et al.* 1992; Madeddu *et al.* 1996; Eva & Solarino 1998; Sue 1998; Sue *et al.* 1999; Volant *et al.* 2000). The parameters of these focal mechanisms are reported in Table 2, while Fig. 5 presents a map showing the available focal mechanisms including the new solutions determined in this study.

Volant *et al.* (2000) propose three different solutions corresponding to three different hypocenter depths, for each of the two events that occurred along the Durance Fault Zone since 1996 (event 961007 and 970208).

We have computed a new focal solution for the event 870509 that has been previously analysed by Béthoux *et al.* (1988) because Nicolas *et al.* (1998) revised its location. The location change implies a change in the focal solution, this new one being more coherent with neighbouring earthquake focal solutions. We did the same operation for the 890212 event, studied previously by Madeddu *et al*. (1996). In that case we obtained a solution similar to the previous one.

In the northeastern part of the studied region, the magnitude 4.7 event n14 (971031) and magnitude 3.6 event n15 (971106) are located around the town of Allos. These earthquakes were analysed by Sue (1998, Sue *et al*. 1999) in parallel with our study. This author computed the focal solution with only the SISMALP network, with stations very close to the epicentres; we studied the same events with all the other networks without the SISMALP data. We propose one focal mechanism given by FPFIT (see Fig. 3), nevertheless the solution computed by Sue, that has been obtained with the SISMALP dense local network, agrees with our set of polarities and provides a similar tectonic result, i.e., same fault kinematics.

III - Inversion of seismic slip-vector dataset to determine the stress state

A - Methodology

To compute the stress states responsible for present-day activity (i.e., for earthquakes) in the studied area, we performed quantitative inversions of the earthquake focal mechanisms, using the method proposed by Carey-Gailhardis & Mercier (1987, 1992) which is one of several existing algorithms (e.g., Vasseur *et al*. 1983; Gephart & Forsyth 1984). For a robust dataset these different algorithms yield similar results (Mercier *et al*. 1991). In appendix A, we succinctly explain the methodology we used to compute the stress states from earthquake focal mechanisms (for more details see Carey-Gailhardis & Mercier 1987, 1992). We complement this appendix explaining how we measured the uncertainties in the preferred direction of the stress state.

B - Results

In the current study we analysed 89 events including the bibliographic and the new focal mechanisms (Tables 1 and 2). However, twenty-five focal mechanisms are not reliable enough to be included in the computed inversions. These are mainly after-shocks, low magnitude events, ill-defined focal mechanisms or solutions from previous studies (870509, 890212, 971031 and 971106). Results of the earthquake slip datum inversion are given in Table 3 with the computed uncertainties for each σ axis and shown with stereoplots on Fig. 6

zone by zone. Histograms showed also the focal depth repartition for each zone. The computed σ_1 and/or σ_3 orientations are shown in map view on Fig. 7 and are discussed below by stress regime and locality. Moreover, in some zones, the focal mechanisms are in agreement with the regional or local tectonic regime but we have not enough events to constrain an inversion. For example, the event n11 (941124), showing an E-striking pure reverse fault and located on the Castellane Thrust, confirms the hypothesis of the southward progression of the Castellane nappe controlled by the Maures Massif position (Ritz 1991).

The results permit us to identify six different tectonic domains, i.e., stress regime zones characterised by a homogeneous deformation field (Fig. 6 and 7), these zones are well defined in term of stress regime (homogeneous stress state) but the boundaries are not well constrained due to the earthquake epicentre location uncertainty. These identified tectonic domains are:

-The Rhone Valley (zone A).

-The Moyenne Durance Fault Zone (zone B).

- A reverse faulting domain north of the Digne nappe (zone C).

- A normal faulting domain north of the Digne nappe (zone D).

- The zone south-east of the Argentera Massif (zone E).

- The Ligurian basin (zone F).

Zone A: The Rhone Valley

In Zone A we compiled four bibliographic and two new mechanisms (see Tables 1 & 2 for references). This small number of focal mechanisms is due (1) to a seismicity gap in the region, and (2) to a lack of stations in the Rhone Valley. However, the inversion of these 6 mechanisms is relatively well-constrained and the result is stable. It is a high quality inversion (100% of (τ , s) angular deviations are lower than 20°, and the confidence cone angle of the of the σ_3 axis do not exceed 20° - see Fig. 6 and Table 3). The inversion result indicates a normal faulting stress regime (σ_1 vertical) with an E-trending σ_3 axis (σ_3: N270°E). We notice that event 16, (840219) of Ml=4.3, is located around Gardanne, east of the Durance Fault, but it is coherent with the regional Rhone Valley stress regime (see the zone A inversion on Fig. 6 and Fig. 7).

Zone B: The Moyenne Durance Fault Zone

Only 5 earthquakes have been compiled along and around this fault zone (including a new one on the margin of the Mediterranean Sea). Nevertheless, they are very consistent with a NNW compression. Inversion of these 5 events provides a high quality result (the confidence cone angle around σ axis is of about 10° - see Table 3) that yields a reverse faulting stress state (σ_3 vertical) characterised by a N158°E-trending σ_1 axis.

Zone C: The Digne Nappe reverse faulting domain

In this zone, corresponding to the Digne and Castellane thrusts, we compiled 12 earthquakes with 5 new solutions. Inversion of these solutions permits us to determine a reverse faulting stress regime with a N046°E-trending σ_1 axis. All the preferred fault planes show an angular deviation between τ and s of less than 10°, indicating that the focal mechanisms are homogeneous and permitting us to compute a high quality inversion (see Table 3).

Zone D: The Digne nappe normal faulting domain

In this area within the Digne nappe, we compiled 14 coherent normal faulting focal solutions, consistent with an extensional tectonic regime. These events are mainly clustered in the northern central part of the Digne nappe. The well-defined inversion of these slip data provides a result corresponding to a normal faulting stress regime with a N102°E-trending σ_3.

Zone E: SE of the Argentera Massif

We divided the earthquakes of the Ligurian zone into two groups. The first one corresponds to the "continental" focal mechanisms of the Ligurian margin, related to the deformation of the SE Argentera Massif. Focal mechanisms of earthquakes, which occur in this zone, are consistent with a strike-slip faulting stress regime (σ_2 vertical). Inversion of these 13 solutions is well-constrained and permits us to characterise a strike-slip stress state with a N155°E-trending σ_1 axis, and a confidence cone angle of about 5° (see Table 3). We note that this determined σ_1 axis is similar to that in zone B, and the average focal depth in this zone is higher than in zone F (see Fig. 6).

Zone F: The Ligurian Basin

In this zone we compiled 14 focal mechanisms. They correspond to the earthquakes in the Ligurian Sea, except events 30 (861029) and 48 (910628) in a transitional zone with zone B. We can identify dip- to oblique-slip reverse and strike-slip faulting. The high quality inversion of these solutions (less than 5° - see Table 3) provides evidence for a reverse faulting stress regime with a N115°E-trending σ_1 axis. This is significantly different from the σ_1 axis determined in zone E with an angular difference of 50°.

IV - Discussion

Eva & Solarino (1998) performed a compilation and an inversion from earthquake focal mechanisms within the Ligurian domain from the Argentera range to the Ligurian Sea. This inversion using the Gephart & Forsyth (1984) method gives a mean stress regime for this wide zone, with a stress ratio defining a reverse faulting stress state with an horizontal σ_1 direction of about N142°E. As mentioned above, for a robust dataset the Gephart & Forsyth (1984) and Carey (Carey-Gailhardis & Mercier 1987) methods yield similar results (see Mercier *et al.* 1991). However, the current analysis using Carey's inversion of the Ligurian domain earthquakes allow us to distinguish two sub-zones (Zones E and F) characterised by homogenous deformation, both zones being coherent with significantly different tectonic regimes. Inversion of the earthquakes located in the basin (zone F) gives a well-defined reverse faulting stress regime with a N115°E-trending σ_1 axis, whereas, the earthquakes affecting the southeast of the Argentera Massif (zone E) are consistent with a strike-slip stress state with a σ_1 axis oriented N155°E. In the Ligurian basin (zone F), the WNW-trending σ_1 does not agree with the N-trending convergence of the Africa plate (DeMets *et al.* 1990, 1994). We can explain this phenomena either by: 1- a local effect of the lateral expulsion of the southwestern Alps along the Apulian indenter (Bethoux *et al.* 1992); or, 2- a reorientation of the maximum stress direction σ_1 orthogonally to the major faults of the Ligurian Sea Margin, as already mentioned for deformation zones around the Mediterranean domain by Rebaï *et al.* (1992). Indeed, they notice a perturbation of the regional stress field close to major faults.

The stress regimes in the southeast of the Argentera Massif (zone E) and around the Durance fault (zone B) are very consistent in direction of compression with coherent NNW-trending σ_1 (N155°E in zone E and N158°E in zone B). However, the deviators acting in both zones define different faulting stress regimes, i.e., a strike-slip-faulting regime and a reverse faulting regime, respectively. The stress state that we determine in zone B is consistent with the geologically determined regime deduced from inversion of striae affecting Pliocene deposits along the Moyenne Durance Fault (i.e., Valensole II Formation) (Baroux 2000, Baroux *et al.* 1999a, 1999b, Bellier *et al.* 1998). This implies a left-lateral component of the present-day reverse oblique-slip of the Moyenne Durance Fault confirmed by the focal mechanisms determined by Volant *et al*. (2000) for the two last earthquakes affecting the fault domain. It does not agree with the present-day right-lateral component recently postulated by Hippolyte (1999) on the basis of a local microtectonic observation.

Major changes in the orientation of the stress axes are determined for very narrow zones, i.e., variation of the stress axes on short distance (zones B (B & E), C, D and A). The maximum stress axis of zones B & E (N155°E & 158°E) is in agreement with the approximately N-trending convergence of the African and Western Europe plates (DeMets *et al*. 1990, 1994), and with geodetic measurements from VLBI in this region (Ward 1994; Zarraoa *et al*. 1994). In contrast, the Digne nappe stress state (zone C) is inconsistent with the stress regimes of zones B and E.

Moreover, the northern part of the Digne nappe, zone D, which have average focal depth corresponds to the E2 zone of Sue's focal mechanisms (Sue 1998, Sue *et al*. 1999). Both the current and the Sue inversions determine normal faulting stress states with an approximately WNW-trending σ_3 axis. An extensional regime has been inferred from the earthquake focal mechanisms within the major part of the western alpine core (Sue 1998; Sue *et al*. 1999). This extensional regime could be due to gravitational body forces related to the Alpine high topography, i.e., a response to buoyancy forces which presently drive the extension of the core of the western Alpine arc.

Conversely, the front of the Digne nappe is characterised by a reverse faulting stress regime with a NE-trending σ_1 axis. The stress state we determined by inversion of seismic slip (earthquake focal mechanisms) in the Digne and Castellane nappes is in close agreement with the geologically determined stress state that has been provided by inversion of slip-vectors (striae) measured along the nappes (Ritz 1991). This similarity strongly suggests that the determined stress states are regionally significant. According to Ritz (1991), the Digne and Castellane thrusts seems shallow and can be considered as flowing toward the open southern basins, i.e., Valensole and Var basins. Moreover, Ritz (1991) explains that the Maures Massif controls the Castellane nappe progression (see on Fig. 1 for location).

Therefore, we can consider the eastern part of Provence, between the Moyenne Durance Fault and the SE of Argentera Massif, as a block (except the Digne and Castellane nappes) which the Africa-Europe convergence controls. The north-east domain of this Provence block is just draped by the Digne and Castellane nappes that are pushed by the core of the western Alpine Arc. The Moyenne Durance Fault kinematics results from the Provence block movement and thus is not influenced by the Digne stress state, even if the Digne Thrust is very close. Consequently, our results suggest that different boundary forces influence the deformation both of the Digne nappe and the Provence block, including the Moyenne Durance fault; i.e., to the north-east, the push of the Alpine front, and to the southeast, the northward African drift.

The stress state in the Rhone valley (zone A) differs drastically from the regimes acting on the other Provence blocks. Indeed, the stress regime determined by seismic slip inversion is clearly extensional with an E-trending σ_3 axis. Around Avignon, two normal-faulting focal mechanisms of Ml=3.1 and Ml=3.6 earthquakes show normal dip-slip on N-striking fault planes, suggesting that the NE-trending Nîmes fault could have presently a normal displacement with a small strike-slip component.

This normal faulting does not agree with the deformation observed in the paleoseismic trench at Courthézon, located in the Rhone valley, about 15 km north to Avignon (Carbon *et al.* 1993; Combes *et al.* 1993; Ghafiri 1995; Blès *et al.* 1995; Sébrier *et al.* 1997). This trench demonstrates a reverse fault affecting a Middle-Riss terrace. The age of these terrace deposits is undefined and only estimated by lithologic correlation and thus it could correspond to early Pleistocene sediments. However, this observation suggests a recent change, i.e., probably in the Quaternary, from a reverse to a normal faulting in stress regime, supporting results of previous faulting analysis in the Rhone valley. Indeed, Blès & Gros (1991) describe N-striking normal faults affecting late Pliocene sediments, with a cumulative displacement of about 20 meters. This confirms a Quaternary E-trending extension acting in the Bas-Dauphiné, between Valence and Vienne (about 45.10°N-5.00°E). This normal faulting is described as subsequent to a regional compression.

This temporal change in stress regime from reverse to normal faulting is consistent with a temporal variation in the magnitude of the maximum horizontal stress. Unfortunately, the timing of the temporal variations in stress state inferred from the geologic/seismic data is too poor to determine if there has been a single recent absolute change in stress magnitude. Nonetheless, the orientation of the E-trending σ_3 axis is coherent with the regional direction of the Africa convergence, toward the NNW.

The Moho discontinuity in the Rhone Valley is 25-km deep, and the Cenozoic sedimentary cover is thick, i.e., about 6-7 km (Hirn, 1980). The continental crust all along the Valley is thus very thin. The high heat flow due to crust thickness could explain the low seismicity we observed. Consequently, aseismic deformations may be efficient in the region. In addition, in the Massif Central, sparse but significant and regular seismicity testifies for an extensional tectonic regime coeval with a regional uplift (Delouis *et al.* 1993). Striae measured on fault planes affecting post-late Miocene deposits indicate a normal faulting stress regime with an ENE-trending extension (Burg & Etchecopar, 1980). This geologically and seismically active extension could result from effects of the mantle plume described under the Massif Central (Granet *et al.* 1995; Sobolev *et al.* 1996; 1997). In fact, it could result from superposition of buoyancy forces related to the mantle upwelling on the regional stress resulting from boundary forces. These resulting extensional Massif Central forces can influence the Rhone Valley domain and produce the present-day stress regime determined by seismic slip inversion.

V - Conclusion

We computed in the current study 17 new focal mechanisms for earthquakes affecting SE France and we compiled 89 earthquakes, including the new solutions between the Alpine and Massif Central fronts up to the Ligurian Sea. We identified 6 different deformation domains corresponding to the main "tectonic regions" of Provence and the Ligurian Sea. Then, performing inversions of the seismic slip-vector (focal solutions) dataset, we determined the stress state characterising of each of these tectonic domains.

Regionally this study allows us to identify two zones around the Provence block characterised by drastically different stress regimes: the western one affected by an extensional stress (normal faulting) regime and an eastern one by a compressional stress (reverse to strike-slip faulting) regime.

The compressional stress field in the Provence domain approximately agrees with the plate convergence between Africa and Europe. The Moyenne Durance Fault movement (reverse with left-lateral strike slip movement) is not controlled by the Digne nappes stress state but directly by the northward drift of the African plate. We thus observed a drastic change of the stress state orientation in a very narrow zone around the Moyenne Durance Fault.

In the Rhone Valley, an E-trending extension characterises the tectonic regime. This extension can be correlated with the uplifted and thin crust of the Massif Central related to an active mantle plume. However, our observations provide evidence for a temporal change in the stress regime from reverse to normal faulting probably during the Pleistocene that is consistent with a temporal variation in the magnitude of the maximum horizontal stress.

In conclusion, this study provides evidence for abrupt spatial stress changes in a narrow zone that reflect abrupt change in the boundary force influences. Indeed, these spatial stress changes around the Provence block result from the coeval influence of forces applied at both its extremities, i.e., to the north-east, the Alpine front push, and to the southeast, the northward African plate drift. Besides these boundary forces, the influence of the mantle plume under the Massif Central, around the western block boundary, could be superimposed. However, these abrupt spatial stress changes in a narrow zone could reflect a tectonic model with upper crustal fragments (blocks) decoupled from the lithospheric mantle by the ductile lower crust as suggested by Müller *et al.* (1997) for short-scale variation of the tectonic regimes acting in western Europe.

Acknowledgements

This study has been realised within the co-operative agreement frames between the IPSN (BERSSIN), CEA (LDG), GéoSciences Azur and OrsayTerre. Special thanks are due to the persons who provided access to the data: Marc Nicolas from LDG, Paolo Augliera from IGG, Michel Granet from ReNaSS, Philippe Volant from IPSN and the SISMALP team. We thank the two anonymous reviewers for their helpful comments, Frédéric Ego for his assistance for the inversions of this study, and Anthony Lomax and Christina Matone for their comments and corrections, which improve considerably this paper. The GeoFrance3D project (MENESR, CNRS, BRGM) and PNRN (INSU-CNRS) supported this work. This publication is the contribution n°85 of GeoFrance3D and n°287 of UMR GéoSciences Azur.

References:

Baroux, E. 2000. Tectonique active en région à sismicité modérée : le cas de la Provence (France). Apport d'une approche pluridisciplinaire. *PhD Thesis*. Univ. Paris-Sud, France. 327 pp.

Baroux, E., Valensise, G., Bellier, O., & Sébrier, M. 1999a. Is the Manosque Anticline (Southeastern France) the Result of Neogene Tectonics along the Moyenne Durance Fault? A geomorphic modelling. *European Union of Geosciences*. Strasbourg, Cambridge Publications, **4**, 1, p. 448.

Baroux, E., Bellier, O., Sébrier, M., Peulvast, J. P., Cushing, M., & Paillou, P. 1999b. Recognition and Characterization of Active Faults in Southwestern France: a

Multidisciplinary Approach. *European Union of Geosciences*. Strasbourg, Cambridge Publications, **4**, 1, p. 553.

Bellier, O., Dumont, J. F., Sébrier, M., & Mercier, J. L. 1991. Geological constraints on the kinematics and fault-plane solution of the Quiches fault zone: reactivated during the 10 November 1946 Ancash earthquake, Northern Peru. *Seis. Soc. Am. Bull.*, **81**, 2, 468-490.

Bellier, O., & Zoback, M.-L. 1995. Recent state of stress change in the Walker Lane zone, western basin and Range province, United States. *Tectonics*, **14**, 3, 564-593.

Bellier, O., Över, S., Poisson, A., & Andrieux, J. 1997. Recent temporal stress state change and modern spatial stress field along the Northern Anatolian Fault Zone, (Turkey). *J. Geophys. Int.*, **131**, 61-86.

Bellier, O., Baroux, E., Sebrier, M., Paillou, P., Cushing, M., & Peulvast, J. P. 1998. L'Identification des failles actives dans le Sud-Est de la France : une analyse morphostructurale sur MNT. *GdR FORPRO - Atelier Thématique 98/IV*. Montpellier, Andra - CNRS.

Béthoux, N., Cattaneo, M., Delpech, P.-Y., Eva, C. & Rehault, J.-P. 1988. Mécanismes au foyer de séismes en Mer Ligure et dans le sud des Alpes occidentales : résultats et interprétations. *C. R. Acad. Sci. Paris*, **307**, Série II, 71-77.

Béthoux, N., Fréchet, J., Guyoton, F., Thouvenot, F., Cattaneo, M., Eva, C., Nicolas, M. & Granet, M. 1992. A Closing Ligurian Sea? *Pure appl. geophys.*, **139**, 179-194.

Blès, J.-L. & Gros, Y. 1991. Stress field changes in the Rhône Valley from the Miocene to the present. *Tectonophysics*, **194**, 265-277.

Blès, J. L., Ghafiri, A., Sébrier, M., Sauret, B., Terrier, M., Godefroy, P., & Martin, C. 1995. Neotectonics and paleosismicity in Provence: contribution to the evaluation of seismic hazard. *Proceedings of the Fifth International Conference on Seismic Zonation*, Nice.

Bossolasco, M., Cicconi, G., Eva., C. & Pasquale, V. 1972. La rete sismica dell'Istituto Geofisico di Genov e primi risultati sulla sismo-tettonica delle Alpi Maritime e Occidentali e del Mar Ligue. *Riv. Ital. Geofis.*, **XXI**, 229-247.

Bott, M. H. P. 1959. The mecanics of oblique slip-faulting. *Geol. Mag.,* **96,** 109-117.

Burg, J. P., & Etchecopar, A. 1980. Determination des systèmes de contraintes liés à la tectonique du Massif Central français : La région de Brioude (Haute-Allier). *C. R. Hebdo. Séances Acad. Sci. Paris,* **290,** Série D, 397-400.

Carbon, D., Combes, P., Cushing, M., & Granier, T. 1993. Enregistrement d'un paléoseisme dans les sédiments du Pléistocène supérieur dans la vallée du Rhône :essai de quantification de la déformation. *Geol. Alpine*, **69**, 33-48.

Carey, E. 1979. Recherche des directions principales de contraintes associées au jeu d'une population de failles. *Revue de Géologie Dynamique et de Géographie Physique*, **21**, 1, 57-66.

Carey, E., & Brunier, B. 1974. Analyse théorique et numérique d'un modèle mécanique élémentaire appliqué à l'étude d'une population de failles. *C. R. Acad. Sc. Paris*, **279**, D, 891-894.

Carey-Gailhardis, E. & Mercier, J.-L. 1987. A numerical method for determining the state of stress using focal mechanisms of earthquake populations: application to Tibetan teleseisms and microseismicity of Southern Peru. *Earth and Planetary Sc. Lett.*, **82**, 165-179.

Carey-Gailhardis, E. & Mercier, J.-L. 1992. Regional state of stress, fault kinematics and adjustments of blocks in a fractured body of rock: application to the microseismicity of the Rhine graben. *J. of Structural Geology*, **14**, 8/9, 1007-1017.

Carey-Gailhardis, E., & Vergely, P. 1992. Graphical analysis of fault kinematics and focal mechanisms of earthquake in terms of stress; the right dihedra method, use and pitfalls. *Annales Tectonicae*, **VI**, 1, 3-9.

Combes, P. 1984. La tectonique récente de la Provence Occidentale : microtectonique, caractéristiques dynamiques et cinématiques. Méthodologie de zonation tectonique et relation avec la sismicité. *PhD Thesis*, Univ. L. Pasteur of Strasbourg, France, 182 pp.

Combes, P., Carbon, D., Cushing, M., Granier, T., & Vaskou, P. 1993. Mise en évidence d'un paléoséisme pléistocène supérieur dans la vallée du Rhône : implications sur les connaissances de la sismicité en France, déformation. *C. R. Acad. Sci. Paris*, **317**, Série IIa, 689-696.

Delouis, B., Haessler, H., Cisternas, A. & Rivera, L. 1993. Stress tensor determination in France and neighbouring regions. *Tectonophysics*, **221**, 413-437.

DeMets, C., Gordon, R. G., Argus, D. F., & Stein, S. 1990. Current plate motions. *Geophys. J. Int.,* **101,** 425-478.

DeMets, C., Gordon, R. G., Argus, D. F., & Stein, S. 1994. Effects of recents revisions to the geomagnetic reversal time scale on estimates of current plate motions. *Geophys. Res. Lett.,* **21,** 2191-2194.

Deverchère, J., Béthoux, N., Hello, Y., Louat, R. & Eva, C. 1991. Déploiement d'un réseau de sismographes sous-marins et terrestres en domaine Ligure (Méditerranée) : campagne SISBALIG 1. *C. R. Acad. Sci. Paris*, **313**, Série II, 1023-1030.

Eva, E. & Solarino, S. 1998. Variations of stress directions in the western Alpine arc. *Geophys. J. Int.*, **135**, 438-448.

Ferhat, G., Feigl, K., Ritz, J.-F. & Souriau, A. 1998. Geodetic measurement of tectonic deformation in the southern Alps and Provence, France, 1947-1994. *Earth and Planetary Sc. L.*, **159**, 35-46.

Fréchet, J. & Pavoni, N. 1979. Etude de la sismicité de la zone briançonnaise entre Pelvoux et Argentera (Alpes Occidentales) à l'aise d'un réseau de stations portable. *Eclogae geol. Helv.*, **72**, 3, 763-779.

Gephart, J. W., & Forsyth, D. W. 1984. An improved for determining the regional stress tensor using earthquake focal mechanism data: an application to the San Fernando earthquake sequence. *J. Geophys. Res.*, **89**, 9305-9320.

Ghafiri, A. 1995. Paléosismicité des failles actives en contexte de sismicité modérée : application à l'évaluation de l'aléa sismique dans le Sud-Est de la France. *Ph.D. Thesis*, Paris-Sud Univ., France.

Granet, M., Stoll, G., Dorel, J., Achauer, U., Poupinet, G., & Fuchs, K. 1995. Massif Central (France): new constraints on the geodynamical evolution from teleseismic tomography. *Geophys. J. Int.*, **121**, 33-48.

Hippolyte, J. C. 1999. The Moyenne Durance active fault (southeastern France) is presently dextral and moving in response to the Alpine push. *European Union of Geosciences*. Strasbourg, Cambridge Publications, **4**, 1, p. 832.

Hirn, A. 1980. Le cadre structural profond d'après les profils sismiques. In *Evolution géologique de la France*. Edited by A. Antran and J. Dercourt. mem. BRGM, **107**, pp. 34-39.

Lee, W. H. & Lahr, J. E. 1975. A computer program for determining hypocenter, magnitude and first motion pattern of local earthquakes. *U.S. Geol. Surv. Open-file rep.*, 75-331.

Levret, A., Backe, J. C. & Cushing, M. 1994. Atlas of macroseismic maps for French earthquakes with their principal characteristics. *Natural Hazards*, **10**, 19-46.

Madeddu, B., Béthoux, N. & Stéphan, J.-F. 1996. Champ de contrainte post-pliocène et déformations récentes dans les Alpes sud-occidentales. *Bull. Soc. géol. France*, **167**, 6, 797-810.

Mercier, J. L., Carey-Gailhardis, E., & Sébrier, M. 1991. Paleostress determinations from fault kinematics: application to the neotectonics of the Hymalaya-Tibet and the Central Andes. *Phil. Trans. R. Soc. Lond.*, **337**, A, 41-52.

Mercier, J.-L., Sébrier, M., Lavenu, A., Cabrera, J., Bellier, O., Dumont, J.-F. & Machare, J. 1992. Changes in Tectonic Regime Above a Subduction Zone of Andean Type: The Andes of Peru and Bolivia During the Pliocene-Pleistocene. *J. Geophys. Res.*, **97**, B8, 11,945-11,982.

Müller, B., Wehrle, V., Zeyen, H., & Fuchs, K. 1997. Short-scale variations of tectonic regimes in the western European stress province north of the Alps and Pyrenees. *Tectonophysics*, **275**, 199-219.

Nicolas, M., Santoire, J. P. & Delpech, P. Y. 1990. Intraplate seismicity: new seismotectonic data in Western Europe. *Tectonophysics*, **179**, 27-53.

Nicolas, M., Béthoux, N. & Mededdu, B. 1998. Instrumental Seismicity of the Western Alps: A Revised Catalogue. *Pure appl. geophys.*, **152**, 707-731.

Reasenberg, P. A. & Oppenheimer, D. 1985. FPFIT, FPPLOT and FPPAGE: Fortran computer programs for calculating and displaying earthquake fault-plain solutions. *U.S. Geol. Surv. Open-file Rep.*, 85-739.

Rebaï, S., Philip, H. & Taboada, A. 1992. Modern tectonic stress field in the Mediterranean region: evidence for variation in stress directions at different scales. *Geophys. J. Int.*, **110**, 106-140.

Ritz, J.F. 1991. Evolution du champ de contraintes dans les Alpes du Sud depuis la fin de l'Oligocène. Implications sismotectoniques. *Ph.D. Thesis*, Univ. of Monpellier II, France, 187 pp.

Sébrier, M., Mercier, J. L., Macharé, J., Bonnot, D., Cabrera, J., & Blanc, J. L. 1988. The state of stress in an overiding plate situated above a flat slab: the Andes of Cenral Peru. *Tectonics*, **7**, 4, 895-928.

Sébrier, M., Ghafiri, A., & Blès, J.-L. 1997. Paleoseismicity in France: Fault trench studies in a region of moderate seismicity. *J. Geodynamics*, **24**, 1-4, 207-217.

Sobolev, S., Zeyen , H., Stoll, G., Werling, F., Altherr, R., & Fuchs, K. 1996. Upper mantle temperatures from teleseismic tomography of French Massif Central including effects of composition, mineral reactions, anharmonicity, anelasticity and partial melt. *Earth Planetary Sci. Lett.*, **139**, 147-163.

Sobolev, S., Zeyen, H., Granet, M., Achauer, U., Bauer, C., F., W., Altherr, R., & Fuchs, K. 1997. Upper mantle temperatures and lithosphere-asthenosphere system beneath the French Massif Central constrained by seismic, gravity, petrologic and thermal observations. *Tectonophysics*, **275**, 143-164.

Sue, C. 1998. Dynamique actuelle et récente des Alpes occidentales internes. *Ph.D. Thesis*, Univ. of Grenoble I, France.

Sue, C., Thouvenot, F., Fréchet, J., & Tricart, P. 1999. Earthquake analysis reveals widespread extension in the core of the western Alps. *J. Geophys. Research.,* **104,** B11, 25,611-25,622.

Vasseur, G., Etchecopar, A., & Philip, H. 1983. Stress state inferred from multiple focal mechanisms. *Ann. Geophys.*, **1**, 291-298.

Volant, P., Berge-Thierry, C., Dervin, P., Cushing, M., Mohammadioun, G. & Mathieu, F. 2000. The South Eastern Durance Fault Permanent Network: Preliminary Results. *J. of Seismology*, **4**, 2, 175-189.

Ward, S. 1994. Constraints on the seismotectonics of the central Mediterranean from Very Long Baseline Interferometry. *Geophys. J. Int.,* **117,** 441-452.

Zarraoa, N., A., R., Sardòn, E., & Ryan, J. 1994. Relative motions in Europe studied with a geodetic VLBI network. *Geophys. J. Int.,* **117,** 763-768.

Appendix A: Methodology of the inversion of seismic slip-vector dataset to determine the stress state

To compute the stress states, we performed quantitative inversions of the earthquake focal mechanisms, using the method proposed by Carey-Gailhardis & Mercier (1987, 1992). This inversion method assumes that the slip (s, represented by a slip-vector corresponding to a striation for geological data or a rake for seismological focal mechanisms) occurs in the direction of the resolved shear stress (τ) on each fault plane, the fault plane being a pre-existing fracture. The inversion computes a mean best-fitting deviatoric stress tensor from a set of fault slip-vectors by minimising the angular deviation between a predicted slip-vector (maximum shear, τ) and the observed slip-vector (s) deduced from the focal mechanism, in the case of a seismic event (Carey & Brunier 1974; Carey 1979). All inversion results include the orientation (azimuth and plunge) of the principal stress axes of a mean deviatoric stress tensor as well as a "stress ratio" $R=(\sigma_2-\sigma_1)/(\sigma_3-\sigma_1)$, a linear quantity describing relative stress magnitudes, where the principal stress axes, σ_1, σ_2 and σ_3, correspond to the compressional, intermediate and extensional deviatoric stress axes, respectively.

To compute stress state from earthquake focal mechanisms it is necessary to know the seismic slip-vector, and consequently to select the preferred seismic fault plane for each pair of nodal planes. For major earthquakes, the selection can be made if there is a co-seismic rupture, or by the spatial epicentre distribution of the aftershock sequence. For earthquake populations characterised by low magnitude and no surface rupture, there exists another alternative, i.e., by computation. Indeed, because only one of the two slip-vectors of a focal mechanism solution is the seismic fault slip-vector in agreement with the principal stress axes, it is possible to compute it following Bott's model (1959). For this slip-vector, the R ratio defined $R=(\sigma_2-\sigma_1)/(\sigma_3-\sigma_1)$, is such that $0<R<1$ (Carey-Gailhardis & Mercier 1987). Moreover, if one of the nodal planes satisfies this condition, the other one does not, except if the both nodal planes of a focal mechanism intersect each other along a principal stress axis (Carey-Gailhardis & Mercier 1987). In this study, to select the seismic fault plane of each focal mechanism, we have used the computation method explained above. Generally, a set of seismic event focal mechanisms leads to a well-defined evaluation of the regional stress state in agreement with the geologically determined stress state, i.e., stress state resulting from inversions of striae measured on fault planes (e.g., Sébrier *et al.* 1988; Bellier *et al.* 1991; Mercier *et al.* 1991, 1992; Bellier & Zoback 1995; Bellier *et al.* 1997).

As mentioned above, fault slip inversion schemes are based on the assumption that the slip direction on each plane represents the direction of the maximum resolved shear stress on that plane. In this case there are 4 unknowns (three defining the orientation of the principal axes and one defining the stress ratio R) and the inversion thus requires at least 4 independent fault sets. Ideal data sets include faults with variable dip angle and with distinct strike directions, not just a continuum of strikes around a single mean direction. A slip-vector, determined from a focal mechanism, is generally considered as mechanically explained by a computed stress deviator when the deviation angle between the calculated slip-vector "τ" and the observed slip-vector "s" is less than 20°. Results of stress inversions are considered reliable if 80% of the deviation angles between τ and s are less than 20° and if the computed solution is stable, i.e., the inversion tends toward the same solution regardless of the initial given parameter values (Carey 1979; Carey-Gailhardis & Mercier 1987, 1992; Mercier *et al.* 1991, Bellier & Zoback 1995).

In addition, for the stress state computation we weighted each fault plane as a function of the earthquake magnitude and focal mechanism quality.

The uncertainties of the stress axes for each zone were calculated computing n inversions with $n-1$ data (if n is the number of data in the conssidered zone) removing one different datum each time, but keeping the same weight. The uncertainty for each σ axis is given in degrees and results from the mean of the angles between the position of σ computed with $n-1$ and n data. It corresponds to the radius of a confidence cone around each σ axis.

In case of earthquakes with multiple solutions, we selected the solution, which is the most coherent with the other mechanisms characterising the surrounding area. To verify this condition, the first stage of the algorithm used is to define compressional and tensional zones by the right dihedral method (Carey-Gailhardis & Vergely 1992), resulting from superimposition of the compressional and tensional quadrants limited by the nodal planes. This preliminary stage permits us to test the homogeneity of the data set used for the inversion. The zones are defined by a trial and error process of mechanism groups allowing the best homogeneity of solutions.

Figure caption

Figure 1: Tectonic map of the area around Provence (modified from Ritz 1991) with the focal solutions (lower hemisphere), computed in this study.

Figure 2: The seismological network available for the south-east France study. The stars are LDG stations, the triangles IPSN stations, the white circles the ReNaSS stations, the crosses the IGG stations and diamonds SISMALP stations. The black dot represents the Gardanne mine, and the rectangular region indicates the location of the earthquakes studied.

Figure 3: Examples of different focal solutions obtained: 1: for the 880805 event a- the graphical solution, b- the 2 solutions obtained with FPFIT code. 2: for the 971106 event a- the graphical solution, b- the FPFIT solution, c- the solution published by Sue et al. (1999).

Figure 4: The detailed focal solutions showing the polarity distributions and multiple solutions if applicable.

Figure 5: The focal solutions collected from literature. The new solutions are reported in grey. DF: Moyenne Durance Fault.

Figure 6: Diagrams of focal mechanisms inversions of Provence earthquakes. Upper histograms show the focal depth repartition in each zone. Small arrows, attached to the fault planes, in the diagrams (Wulff stereonet, low hemisphere) show the slip-vector direction.

White and black arrows indicate the σ_1 and σ_3 axis directions, respectively. Lower histograms give the angular deviation between the predicted slip-vector "τ" and the observed slip-vector "s". They do not take into account the weight of each datum. Numbers correspond to the labels in Tables 1 & 2. To differentiate a new solution from old ones, we add a "9" at the new event labels. For the corresponding zones (A to F), see the text, and Fig. 7.

Figure 7: Distributions of stress orientations in the different zones of Provence. White and black arrows indicate the σ_1 and σ_3 axis directions, respectively. Dots correspond to earthquake locations and DF is for Durance Fault. For the corresponding zones (A to F), see the text. These zones are well-defined in terms of stress regime but the boundaries are not well constrained because of the epicentral location. The inset in the upper-left: I: Extensional tectonic region; II: Africa/Europe convergence influence zone; III: Alpine influence zone.

Table caption

Table 1: Locations and parameters of focal mechanisms obtained in this study. For the corresponding zones, see the text.

Table 2: Locations and parameters of focal mechanisms from the authors of the reference literature (Bo: Bossolasco *et al.* 1972; F: Fréchet & Pavoni 1979; B1: Béthoux *et al* 1988; N: Nicolas *et al.* 1990; D: Deverchère *et al.* 1991; B2: Béthoux *et al.* 1992; M: Madeddu *et al.* 1996; S; Sue *et al.* 1999; V: Volant *et al.* 2000; E: Dister in Eva & Solarino 1998). For the corresponding zones, see the text.

Table 3: Results of regional stress tensor inversions from the significant focal mechanisms in each zone around the Provence block. N corresponds to the number of focal mechanisms used for the inversions. Deviatoric principal stress axes σ_1, σ_2, σ_3, are the compressional, intermediate and extensional deviatoric axes, respectively. They are specified by azimuths (Az) measured clockwise from North, plunges (dip) are measured from horizontal. Δ is the angular deviation corresponding to the radius in degrees of a confidence cone around each σ axis. $R=(\sigma_2-\sigma_1)/(\sigma_3-\sigma_1)$, the "stress ratio" of the deviatoric stress tensor. For the corresponding zones, see the text. For explanation of the calculation methodology see Appendix A.

Figure 1

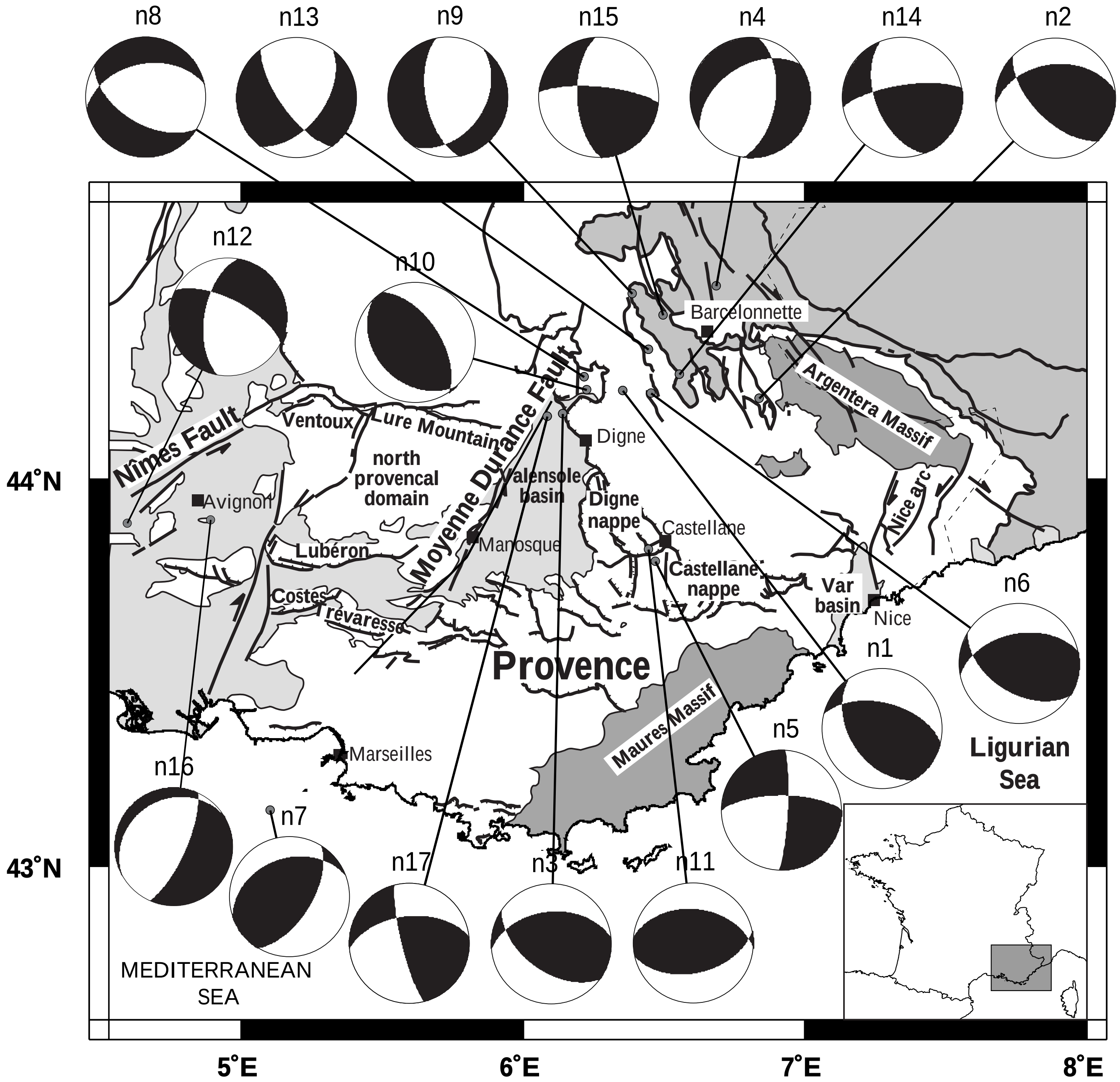

n8
n13
n9
n15
n4
n14
n2
n12
n10
n6
n1
n5
n16
n7
n17
n3
n11
Barcelonnette
Digne
Castellane
Nice
Avignon
Manosque
Marseilles
Nîmes Fault
Ventoux
Lure Mountain
Moyenne Durance Fault
north provencal domain
Valensole basin
Digne nappe
Castellane nappe
Var basin
Argentera Massif
Nice arc
Lubéron
Costes
Trévaresse
Provence
Maures Massif
Ligurian Sea
MEDITERRANEAN SEA
44°N
43°N
5°E
6°E
7°E
8°E

Figure 2

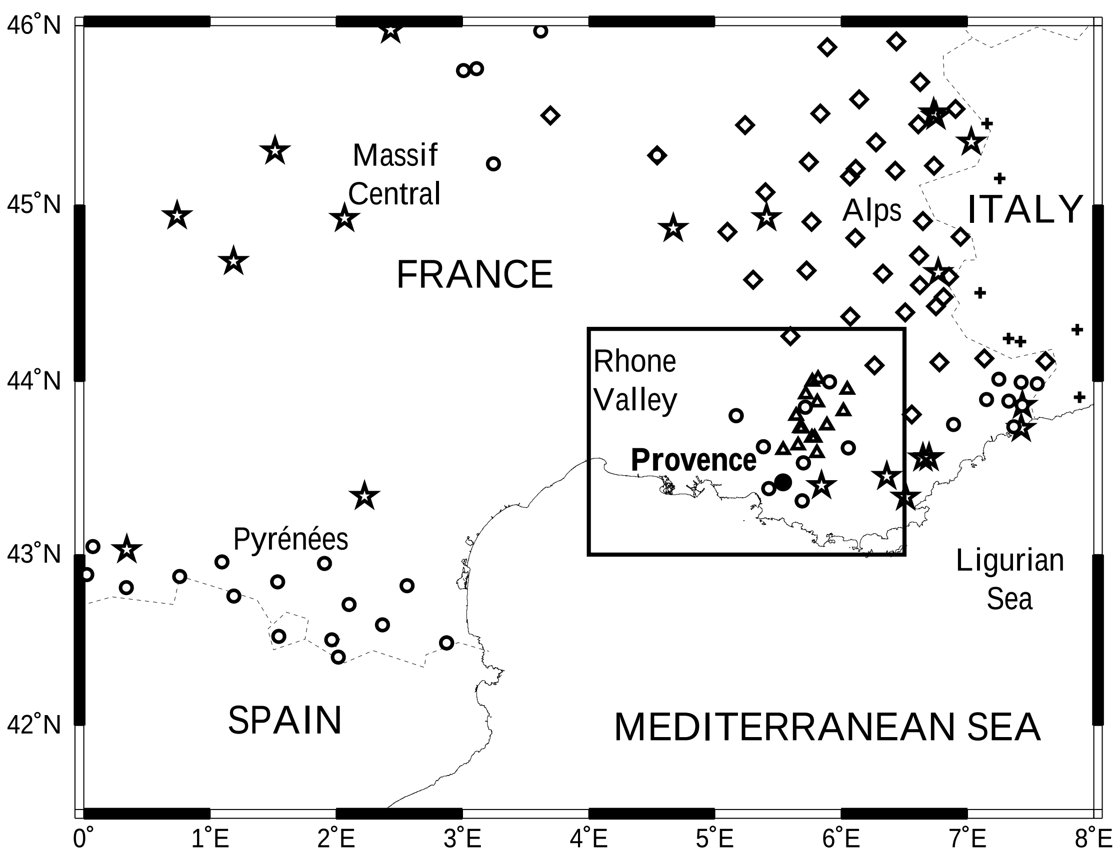

46°N
45°N
44°N
43°N
42°N
0°
1°E
2°E
3°E
4°E
5°E
6°E
7°E
8°E
Massif
Central
FRANCE
Alps
ITALY
Rhone
Valley
Provence
Pyrénées
Ligurian
Sea
SPAIN
MEDITERRANEAN SEA

Figure 3

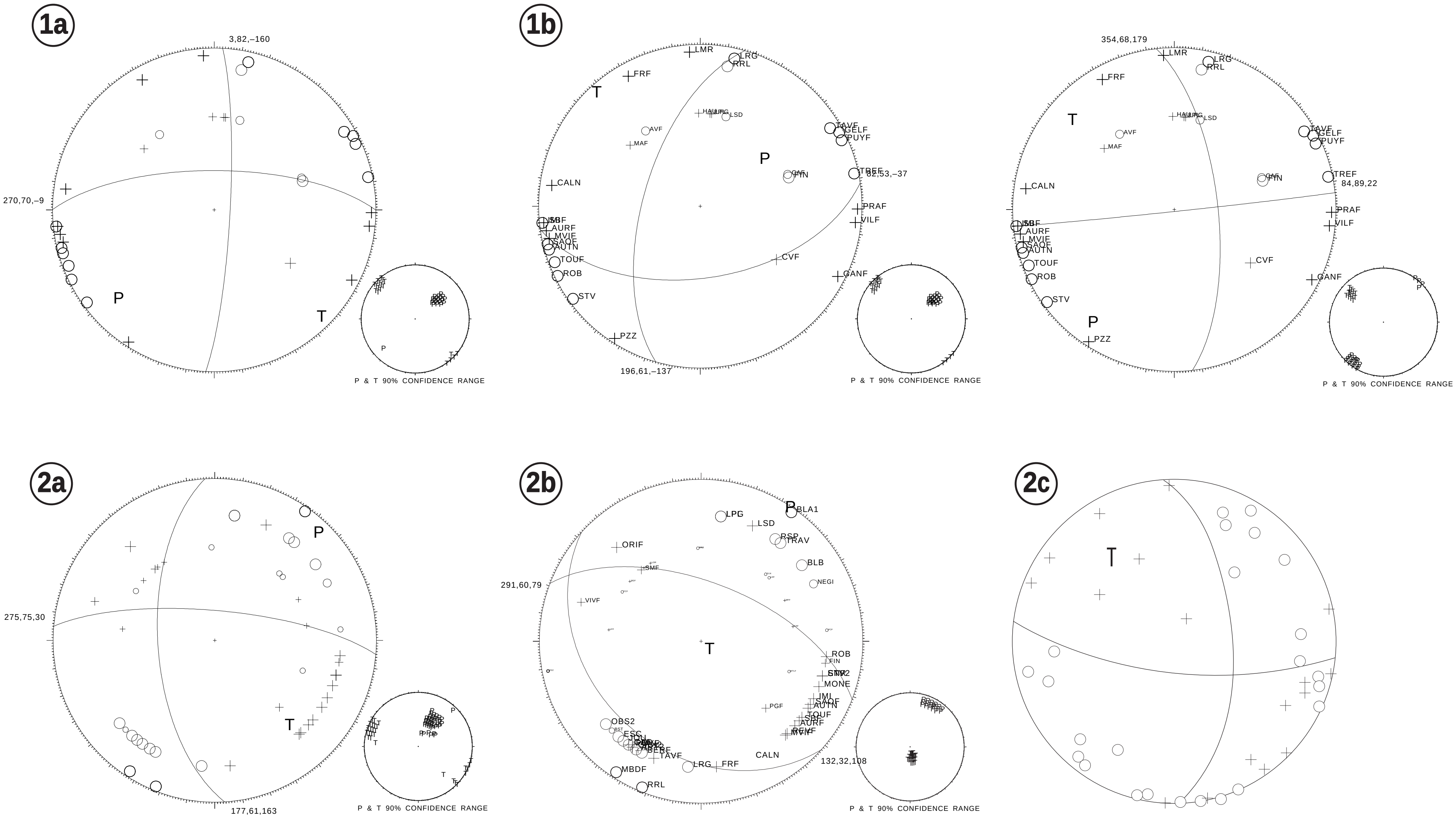

1a
3,82,–160
270,70,–9
P
T
P & T 90% CONFIDENCE RANGE
1b
LMR
LRG
RRL
FRF
T
AVF
MAF
LSD
TAVF
GELF
PUYF
P
TREF
82,53,–37
CALN
PRAF
VILF
AURF
MVIF
SAOF
AUTN
TOUF
ROB
CVF
GANF
STV
PZZ
196,61,–137
P & T 90% CONFIDENCE RANGE
354,68,179
84,89,22
P & T 90% CONFIDENCE RANGE
2a
275,75,30
177,61,163
P & T 90% CONFIDENCE RANGE
2b
LPG
LSD
BLA1
ORIF
RSP
TRAV
BLB
SMF
NEGI
291,60,79
VIVF
T
ROB
FIN
MONE
PGF
SAOF
AUTN
TOUF
AURF
OBS2
ESC
TAVF
LRG
FRF
CALN
MBDF
RRL
132,32,108
P & T 90% CONFIDENCE RANGE
2c
T

Figure 4

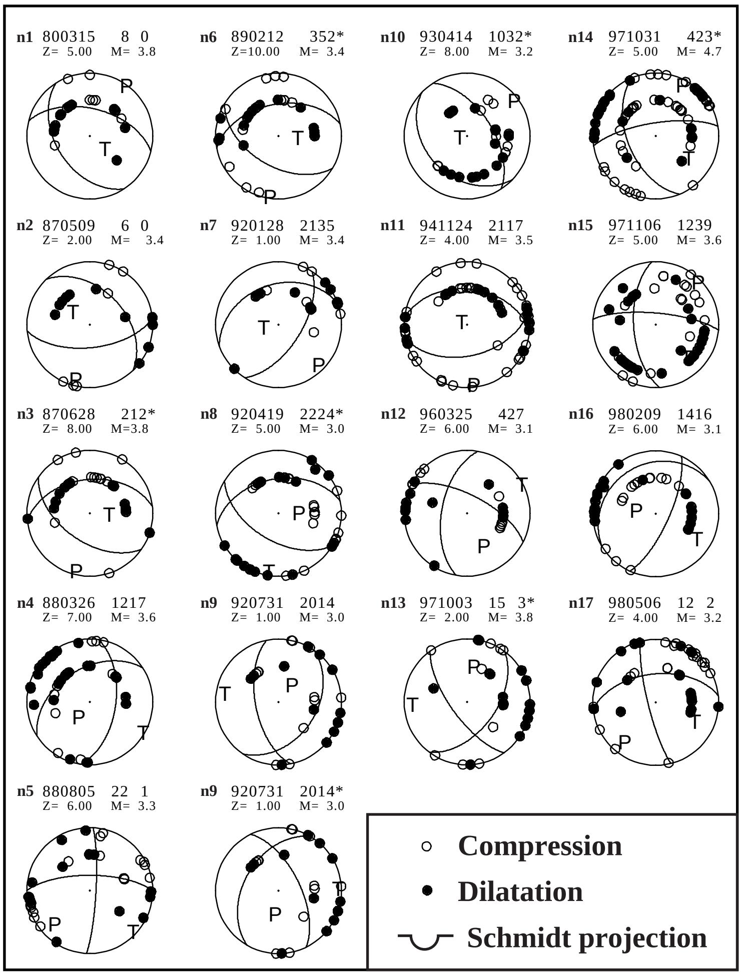

n1 800315 8 0
Z= 5.00 M= 3.8
n6 890212 352*
Z=10.00 M= 3.4
n10 930414 1032*
Z= 8.00 M= 3.2
n14 971031 423*
Z= 5.00 M= 4.7
n2 870509 6 0
Z= 2.00 M= 3.4
n7 920128 2135
Z= 1.00 M= 3.4
n11 941124 2117
Z= 4.00 M= 3.5
n15 971106 1239
Z= 5.00 M= 3.6
n3 870628 212*
Z= 8.00 M=3.8
n8 920419 2224*
Z= 5.00 M= 3.0
n12 960325 427
Z= 6.00 M= 3.1
n16 980209 1416
Z= 6.00 M= 3.1
n4 880326 1217
Z= 7.00 M= 3.6
n9 920731 2014
Z= 1.00 M= 3.0
n13 971003 15 3*
Z= 2.00 M= 3.8
n17 980506 12 2
Z= 4.00 M= 3.2
n5 880805 22 1
Z= 6.00 M= 3.3
n9 920731 2014*
Z= 1.00 M= 3.0
Compression
Dilatation
Schmidt projection

Figure 5

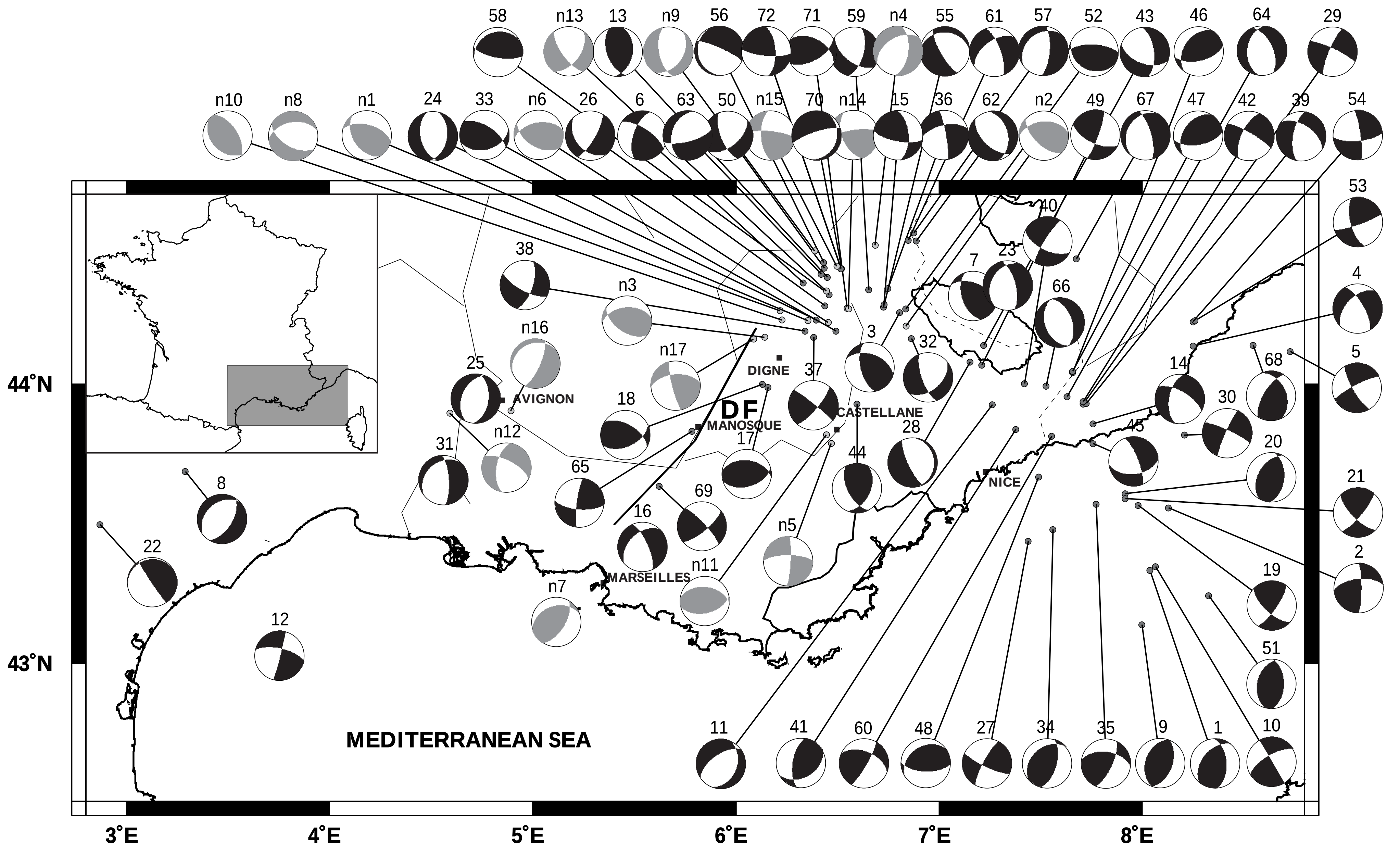

DIGNE
DF
CASTELLANE
AVIGNON
MANOSQUE
NICE
MARSEILLES
MEDITERRANEAN SEA
44°N
43°N
3°E
4°E
5°E
6°E
7°E
8°E

Figure 6

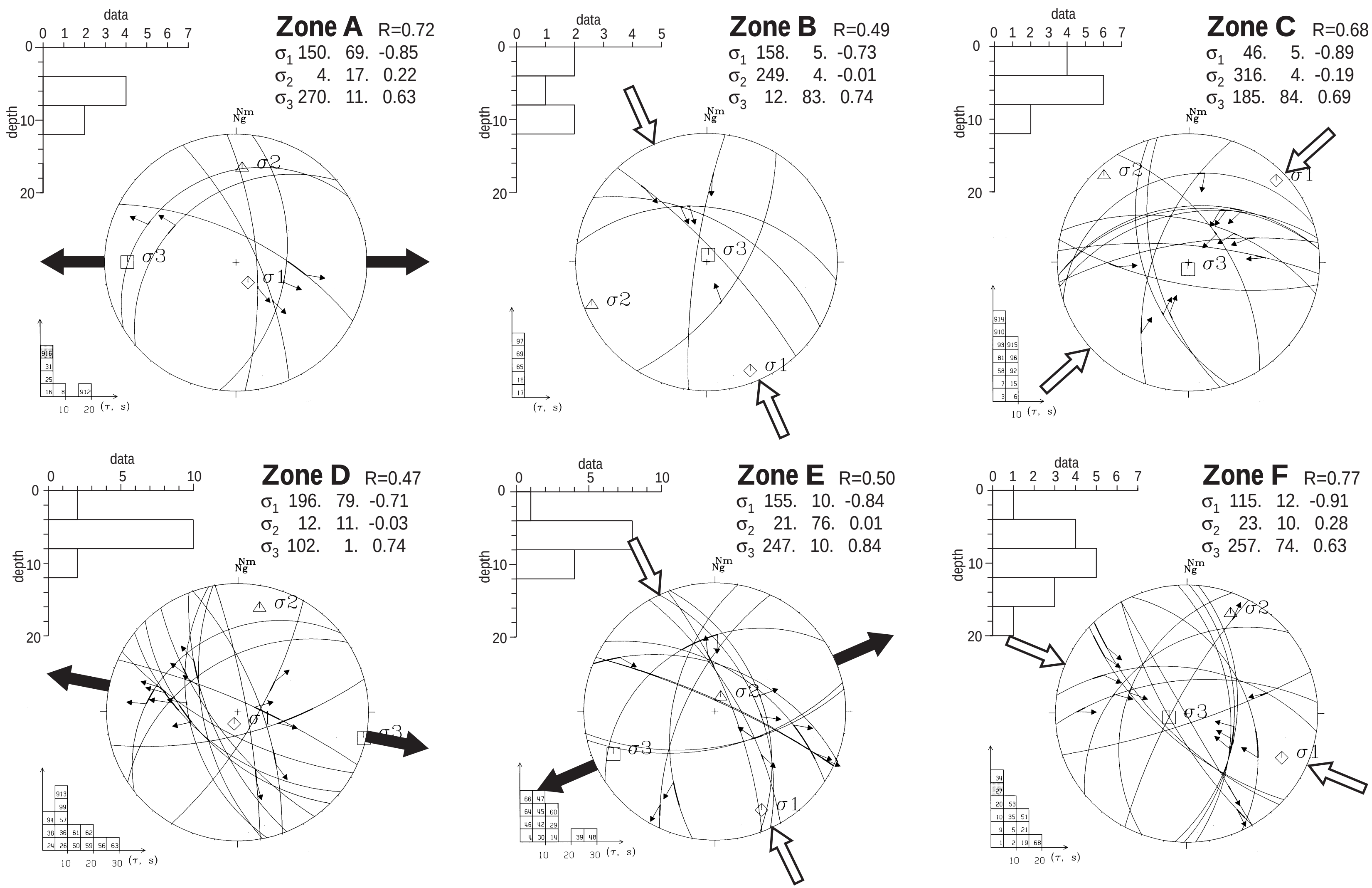
Zone A R=0.72
σ1 150. 69. -0.85
σ2 4. 17. 0.22
σ3 270. 11. 0.63
Zone B R=0.49
σ1 158. 5. -0.73
σ2 249. 4. -0.01
σ3 12. 83. 0.74
Zone C R=0.68
σ1 46. 5. -0.89
σ2 316. 4. -0.19
σ3 185. 84. 0.69
Zone D R=0.47
σ1 196. 79. -0.71
σ2 12. 11. -0.03
σ3 102. 1. 0.74
Zone E R=0.50
σ1 155. 10. -0.84
σ2 21. 76. 0.01
σ3 247. 10. 0.84
Zone F R=0.77
σ1 115. 12. -0.91
σ2 23. 10. 0.28
σ3 257. 74. 0.63
data
depth
Nm
Ng
σ1
σ2
σ3
(τ, s)

Figure 7

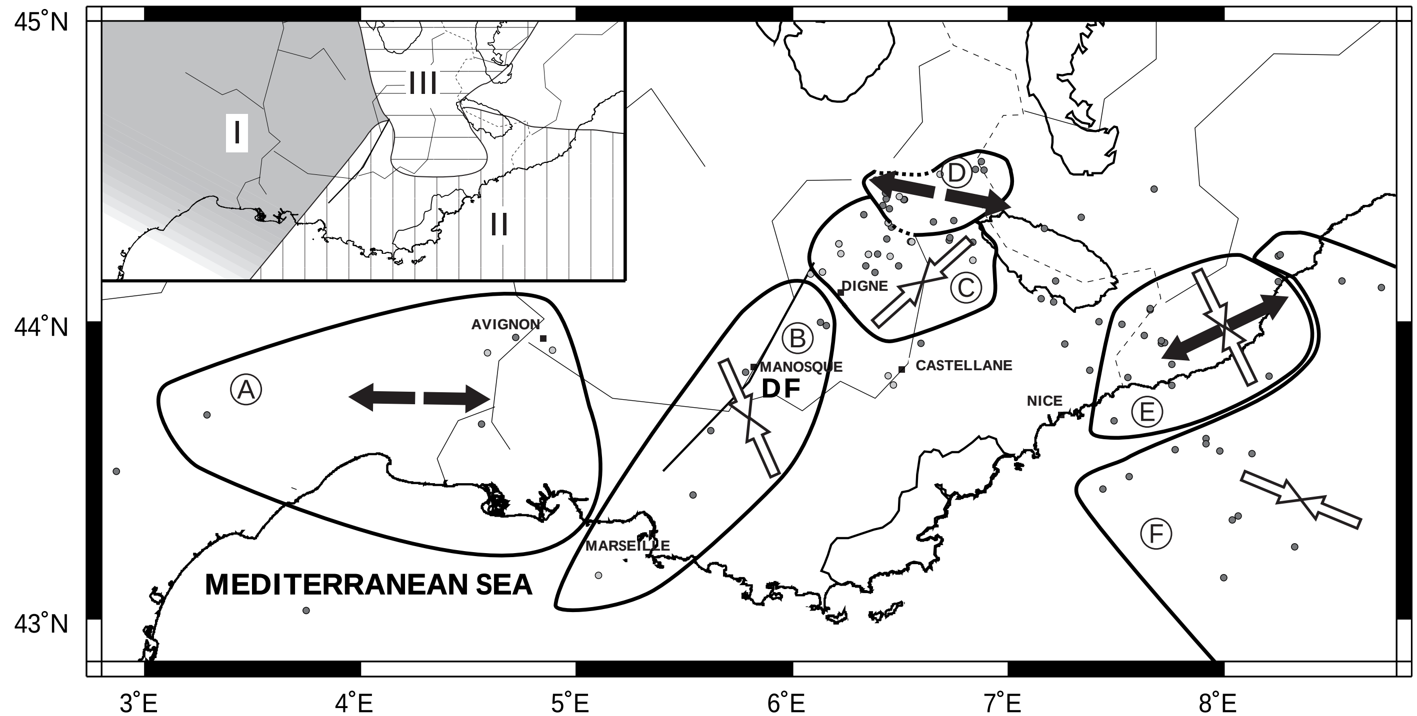

45°N
44°N
43°N
3°E
4°E
5°E
6°E
7°E
8°E
I
II
III
A
B
C
D
E
F
AVIGNON
MANOSQUE
DF
DIGNE
CASTELLANE
NICE
MARSEILLE
MEDITERRANEAN SEA

Table 1

No.	Zone	DATE	Time	Longitude	Latitude	Ml	Depth	Plane A			Plane B			P axe		Taxe	
		yymmdd	*hh:mm:ss*	*°E*	*°N*		*km*	*Az.*	*Dip*	*Rake*	*Az.*	*Dip*	*Rake*	*Az.*	*Dip*	*Az.*	*Dip*
n1	C	800315	08:00:47.86	6,3528	44,2248	3,8	5	147	45	124	284	54	61	034	05	135	67
n2	C	870509	06:00:16.74	6,8377	44,2050	3.4	0,5	316	43	133	084	60	57	197	10	304	60
n3	C	870628	02:12:52.84	6,1410	44,1668	4,0	1	125	53	118	264	45	58	194	04	095	68
n4	D	880326	12:17:10.29	6,6862	44,4912	3.7	7	008	56	-57	237	46	-129	222	63	121	06
n5		880805	22:01:33.25	6,4690	43,7877	3.6	5	270	70	-171	003	82	-20	228	20	135	08
n6	C	890212	03:52:03.45	6,4542	44,2198	3.8	10	259	48	59	121	50	120	190	01	097	67
n7	B	920128	21:35:05.38	5,1043	43,1460	3,4	0,5	250	36	122	032	60	69	137	13	260	67
n8		920419	22:24:53.25	6,2155	44,2607	3.0	5	121	54	-118	259	44	-57	089	67	192	05
n9	D	920731	20:14:27.46	6,3883	44,4722	3,0	0,5	035	39	-129	169	60	-63	033	64	278	12
n10	C	930414	10:32:06.79	6,2272	44,2285	3.2	3	134	34	79	327	57	97	052	11	260	77
n11		941124	21:17:35.41	6,4443	43,8198	3,5	1,5	077	49	77	276	43	105	176	03	285	80
n12	A	960325	04:27:32.62	4,7263	43,9135	3,1	6	190	57	-151	297	66	-37	157	42	062	05
n13	D	971003	15:03:35.44	6,4440	44,3303	3,8	0,5	037	52	-153	144	69	-41	007	43	267	11
n14	C	971031	04:23:43.42	6,5545	44,2660	4,7	5	158	53	159	261	73	39	025	13	126	39
n15	C	971106	12:39:48.69	6,4975	44,4178	3,6	5	177	61	163	275	75	30	043	10	139	31
n16	A	980209	14:16:56.35	4,8913	43,9055	3,1	6	024	73	-78	239	21	-123	277	60	123	27
n17		980506	12:02:26.22	6,0858	44,1605	3,2	4	166	80	142	264	53	13	221	18	118	34

Table 2 (1/2)

No.	Zone	DATE	Time	Longitude	Latitude	Ml	Depth	Plane A			Plane B			P axe		Taxe		Ref.
		yymmdd	*hh:mm:ss*	*°E*	*°N*		*km*	*Az.*	*Dip*	*Rake*	*Az.*	*Dip*	*Rake*	*Az.*	*Dip*	*Az.*	*Dip*	
1	F	630719	05:46:04.0	8,0390	43,3360	6.0	14	356	53	060	220	46	124	107	04	205	66	Bo
2	F	630727	05:57:00.0	8,1300	43,5600	4,8	14	000	80	031	264	61	168	129	13	226	28	D
3	C	691122	07:49:15.0	6,8060	44,2550	3.6	7	166	60	127	290	46	044	231	08	128	58	F
4	E	701230	02:20:00.0	8,2530	44,1380	4,0	5	224	52	-155	330	70	-041	193	42	093	11	D
5	F	710925	10:34:00.0	8,7300	44,1170	4,2	5	150	75	-169	243	80	-015	107	18	016	04	D
6	C	720619	04:09:51.0	6,3330	44,3600	3.8	2	199	60	153	303	67	033	070	05	163	39	F
7	C	721229	00:14:17.0	7,1690	44,3140	3.6	9	295	48	054	162	52	123	229	03	134	64	F
8	A	780829	22:23:48.1	3,2900	43,6900	4.1	8	032	57	-080	230	34	-105	272	76	129	12	N
9	F	810105	08:10:00.0	8,0000	43,1410	3,6	10	020	50	090	200	40	090	110	05	290	85	D
10	F	810422	04:26:21.0	8,0650	43,3490	4.5	9	240	68	-180	150	90	-000	103	15	197	15	B1
11		820902	21:45:25.0	7,2630	43,9280	3.3	10	235	60	-109	020	35	-060	185	69	311	13	B1
12		821223	14:48:13.8	3,7500	43,0300	4.1	6	014	88	-027	283	67	-178	242	20	145	17	N
13		830320	16:01:31.1	6,4500	44,3800	3.9	6	010	40	114	160	54	071	263	07	018	73	N
14	E	831204	17:34:51.0	7,7590	43,8600	3.5	4	190	54	-148	300	65	-041	160	46	063	07	B1
15	C	831222	18:12:21.0	6,7280	44,2750	3.5	6	356	57	155	100	70	036	226	08	322	39	B1
16	A	840219	21:14:37.7	5,5400	43,4200	4.3	8	226	44	-153	336	72	-049	204	47	095	17	N
17	B	840619	11:40:37.1	6,1600	43,9900	4.1	10	278	44	109	073	49	073	175	02	276	77	N
18	B	840630	19:34:05.8	6,1300	44,0000	3.8	6	300	55	129	065	51	048	003	02	269	59	N
19	F	851004	13:17:21.5	7,9800	43,5700	4.0	10	132	66	017	035	75	155	085	06	352	28	N
20	F	851004	15:22:11.0	7,9160	43,6100	3.9	14	210	45	108	005	48	073	107	01	204	77	B1
21	F	851005	15:58:40.0	7,9160	43,5930	3.1	11	040	77	159	135	69	014	088	05	356	24	B1
22		860115	22:19:18.6	2,8700	43,5000	3.7	2	146	86	099	261	09	025	228	40	065	48	N
23		860117	18:48:03.0	7,3390	44,3510	3.3	6	210	33	-130	345	65	-067	219	63	092	17	B1
24	D	860117	20:27:19.0	6,3960	44,2290	3.6	6	010	43	-107	167	49	-075	013	78	268	03	B1
25	A	860225	17:10:39.9	4,7200	43,9500	3.6	5	203	43	-102	007	48	-079	212	82	105	03	N
26	D	860323	13:59:23.9	6,4400	44,2800	3.7	7	140	40	-025	030	74	-127	339	47	093	20	N
27	F	860501	00:28:01.8	7,4400	43,4400	3.8	5	115	78	166	208	78	012	341	00	007	17	N
28		860818	11:37:12.0	7,1550	44,0810	3.2	6	155	75	-085	355	15	-109	065	60	245	30	B1
29	E	861020	20:29:11.0	7,7090	43,9300	3.0	2	203	79	-170	295	80	-011	159	15	069	01	B1
30	E	861029	08:13:34.0	8,2100	43,8210	3.0	10	204	84	-171	295	81	-006	159	11	250	02	B1
31	A	870205	09:59:37.8	4,5600	43,6600	3.5	5	356	72	-067	230	29	-140	236	57	104	24	N
32		870509	06:00:17.0	6,8650	44,1640	3.4	6	050	47	-152	160	70	-047	025	47	280	14	B1
33		890212	03:52:03.7	6,4930	44,1900	3.8	9	302	60	119	074	41	050	012	10	261	63	M
34	F	891226	19:59:59.0	7,5610	43,4830	4.5	4	015	60	070	231	36	121	119	13	244	68	B2
35	F	900415	07:50:36.0	7,7740	43,5740	4.3	5	025	70	042	278	51	154	148	12	259	43	B2
36	D	900507	14:20:51.7	6,7480	44,3400	2.9	5	255	58	-171	350	82	-032	217	28	118	16	M

Table 2 (2/2)

No.	Zone	DATE	Time	Longitude	Latitude	Ml	Depth	Plane A			Plane B			P axe		Taxe		Ref.
		yymmdd	*hh:mm:ss*	*°E*	*°N*		*km*	*Az.*	*Dip*	*Rake*	*Az.*	*Dip*	*Rake*	*Az.*	*Dip*	*Az.*	*Dip*	
37		900629	01:19:00.0	6,3840	44,1670	3.1	6	309	86	166	040	76	004	355	07	264	13	D
38	D	900629	08:55:00.0	6,3420	44,1900	2.8	6	018	64	-158	118	70	-028	340	33	247	04	D
39	E	900702	18:42:00.0	7,7250	43,9320	2.7	4	190	63	-137	303	53	-035	152	49	249	06	D
40		900809	19:16:57.6	7,4200	44,0030	3.2	6	116	60	-168	212	80	-031	078	29	341	13	M
41		900908	08:31:22.9	7,3800	43,8400	2.7	11	060	40	132	190	62	061	301	12	053	61	M
42	E	901002	02:06:24.1	7,7100	43,9400	2.9	11	300	80	-027	205	64	-169	165	26	070	11	M
43		901022	02:11:08.8	7,2200	44,1400	3.0	4	353	60	-134	110	52	-039	053	05	317	52	M
44		901109	10:59:02.6	6,5980	43,9300	3.3	2	152	58	055	025	46	133	266	07	008	60	M
45	E	910205	09:06:10.3	7,7600	43,7900	3.0	8	339	75	-136	083	48	-020	296	40	037	17	M
46	E	910219	15:33:00.0	7,6580	44,0430	3,0	7	215	40	055	077	58	115	149	10	036	66	M
47	E	910225	11:30:11.8	7,6600	44,0480	3.3	4	215	40	053	080	59	117	151	10	038	64	M
48	E	910628	23:48:48.0	7,4900	43,6700	2.9	5	092	62	108	237	33	060	169	15	038	68	M
49		910714	20:47:50.5	7,2100	44,0700	2.9	5	020	81	151	115	61	010	071	13	334	27	M
50	D	920102	02:12:00.0	6,4350	44,4130	2.3	8	050	55	-030	158	66	-141	018	44	282	07	S
51	F	920921	12:37:04.0	8,3278	43,2445	3,0	20	000	50	080	195	41	101	097	05	217	81	D
52		930505	04:34:00.0	6,8370	44,2680	1.2	10	115	25	110	273	67	081	010	21	166	67	S
53	F	930717	10:35:00.6	8,2525	44,2215	4,5	8	165	65	009	071	81	155	120	11	025	24	D
54		930717	11:08:23.2	8,2623	44,2273	3,7	9	085	70	-009	352	81	-160	307	21	040	07	D
55		940415	02:58:00.0	6,7310	44,2830	1.8	6	150	75	-110	275	25	-038	085	56	224	27	S
56	D	940627	17:48:00.0	6,4330	44,4330	2.7	7	165	15	-140	294	80	-078	190	53	034	34	S
57	D	940924	04:18:00.0	6,8770	44,5360	2.5	4	005	70	-070	232	28	-133	246	60	110	22	S
58	C	941113	00:36:00.0	6,4610	44,3180	1.4	7	100	70	100	253	22	064	182	24	026	64	S
59	D	941128	08:28:00.0	6,6560	44,3370	1.8	9	015	60	-140	128	56	-037	340	48	072	02	S
60	E	950421	08:02:57.5	7,5563	43,8155	4,3	4	030	80	039	292	51	167	155	19	259	35	D
61	D	951013	22:07:00.0	6,8490	44,5110	2.9	6	340	70	-040	234	53	-155	203	42	103	11	S
62	D	951018	02:13:00.0	6,8880	44,5090	2.1	4	135	55	-070	347	40	-116	354	72	239	08	S
63	D	960809	17:31:00.0	6,4190	44,3910	1.7	7	075	70	-120	196	36	-036	023	55	143	19	S
64	E	960926	21:37:36.7	7,6307	43,9562	2,7	7	187	40	-116	335	55	-070	194	72	079	08	D
65	B	961007	12:26:27.9	5,7845	43,8335	2,9	3	094	67	169	188	80	023	319	09	053	23	V
66	E	961017	15:21:38.8	7,5287	43,9953	3,2	10	160	40	-090	340	50	-090	250	85	070	05	D
67		961124	00:27:08.1	7,6783	44,4450	3,5	3	212	27	-135	344	71	-070	226	59	089	23	D
68	F	961125	19:47:23.2	8,5465	44,1390	3,8	3	335	40	040	212	66	123	278	14	165	58	D
69	B	970208	19:18:42.8	5,6228	43,6370	2,9	9	050	73	011	317	79	163	004	05	273	19	V
70		971022	04:51:00.0	6,5210	44,4100	2.1	9	020	20	-040	252	77	-106	181	55	329	31	S
71		971031	04:23:00.0	6,5470	44,2710	4.0	5	060	60	050	299	48	138	177	07	277	55	S
72		971106	12:39:00.0	6,5180	44,4110	3.1	9	095	75	030	357	61	163	223	09	319	32	S

Table 3

Zone	N	σ_1			σ_2			σ_3			R value
		Az.	*Dip*	*Δ(°)*	*Az.*	*Dip*	*Δ(°)*	*Az.*	*Dip*	*Δ(°)*	
A	6	150	69	20	004	17	11	270	11	9	0,72
B	5	158	05	8	249	04	23	012	83	15	0,49
C	12	046	05	1	316	04	2	185	84	5	0,68
D	14	196	79	5	012	11	3	102	01	2	0,47
E	13	155	10	3	021	76	5	247	10	3	0,51
F	14	115	12	2	023	10	2	257	74	3	0,78